JACS
JOURNAL OF THE AMERICAN CHEMICAL SOCIETY

ARTICLE

pubs.acs.org/JACS

Atomistic Structure of a Micelle in Solution Determined by Wide *Q*-Range Neutron Diffraction

Rowan Hargreaves,*[,†] Daniel T. Bowron,[†] and Karen Edler[‡]

[†]STFC—ISIS Neutron Scattering Facility, Didcot, United Kingdom

[‡]Department of Chemistry, University of Bath, Bath, United Kingdom

Supporting Information

ABSTRACT: The accepted picture of the structure of a micelle in solution arises from the idea that the surfactant molecules self-assemble into a spherical aggregate, driven by the conflicting affinity of their head and tail groups with the solvent. It is also assumed that the micelle's size and shape can be explained by simple arguments involving volumetric packing parameters and electrostatic interactions. By using wide *Q*-range neutron diffraction measurements of H/D isotopically substituted solutions of decyltrimethylammonimum bromide (C_{10}TAB) surfactants, we are able to determine the complete, atomistic structure of a micelle and its surroundings in solution. The properties of the micelle we extract are in agreement with previous experimental studies. We find that ∼45 surfactant molecules aggregate to form a spherical micelle with a radius of gyration of 14.2 Å and that the larger micelles are more ellipsoidal. The surfactant tail groups are hidden away from the solvent to form a central dry hydrophobic core. This is surrounded by a disordered corona containing the surfactant headgroups, counterions, water, and some alkyl groups from the hydrophobic tails. We find a Stern layer of 0.7 bromide counterion per surfactant molecule, in which the bromide counterions maintain their hydration shells. The atomistic resolution of this technique provides us with unprecedented detail of the physicochemical properties of the micelle in its solvent.

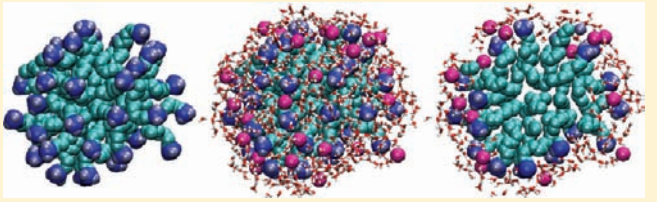

INTRODUCTION

The dramatic increase in the application of micelles, and other self-assembled structures, in nanotechnology is stimulating significant scientific interest. Through the manner of their preparation, the size and shape of these self-assembled structures can be tuned for a variety of different purposes. Applications of particular current interest are as nanocarriers, where they encapsulate other chemical species, and as soft-templates, where they direct the bottom-up assembly of nanostructured materials.

Surfactant micelles play an important part in a large number of well-established and emerging technologies. The chemical and consumer product industries have long employed micelles, and polymer−micelle mixtures, in paints, coatings, adhesives, cosmetics, and many other household products. In addition, they are used in the processes of enhanced oil recovery (e.g., micelle−polymer flooding) and in environmental cleanup of pollutants.[1,2] These mixtures have found such considerable application because the interaction of the polymers and the micelles allows the mixtures' properties to be tailored in desirable ways. For example, the viscosity of polymer−micelle solutions can be made significantly greater than that possible in either polymer-only or micelle-only solutions.[3] Another useful property of micelles is that they can incorporate other chemical species into their structure. This allows them to act as reaction media and thereby modify the reaction rate and routes of a chemical reaction in a favorable manner.[4] Similarly, the idea of solubilizing therapeutic molecules in micelles is receiving considerable current research effort. It is hoped that, by acting as a drug or gene delivery vector, micelles and other aggregates can prolong a drug's release rate, increase its specificity, and reduce its toxicity.[5,6] Also, an increasing range and diversity of new mesoporous materials are being synthesized by using micelles as supramolecular templates, allowing the pore size, shape, and roughness to be designed for a particular use—in solar cells, batteries, molecular sieves, or catalysts.[7,8] Clearly, to design, or tune, the self-assembled aggregates employed in any of these applications requires a detailed, atomistic understanding of their physicochemical properties and their interaction with the solvent and any cosolutes.

The exact size and morphology of a micelle are determined by a number of factors, including the type of surfactant, its concentration, the temperature, the pH, and the action of salt, other solutes, and cosolvents.[9] For ionic surfactants the electrostatic repulsion between the headgroups counterbalances the aggregation of the tail groups. It is thought that a fraction of the counterions bind to the surface of the micelle, forming a layer known as the Stern layer, and in doing so, they screen the charges of the headgroups, allowing them to pack more closely together.

Received: June 22, 2011
Published: August 08, 2011

The *n*-alkytrimethylammonium bromide (C_nTAB or TAB) surfactants are a class of cationic surfactants that have received extensive study. The TABs are commonly used as templates for porous inorganic oxides and as components of fabric softners, hair conditioners, and lubricants. In addition, the TABs, along with their anionic cousin, sodium dodecyl sulfates, are considered model amphiphiles. C_{10}TAB, the smallest micelle-forming TAB, is less studied than the longer tailed TABs because it is more expensive and less used commercially. From experimental studies the average number of surfactant molecules in a C_{10}TAB micelle at 298 K has been reported in the range of 37 molecules[10] to 50 molecules.[11] The micelle is considered to be spherical[12,13] with a radius of just under 18 Å.[14,15] Between 0.78 and 0.58 of the bromide counterions are found to be bound to the outside of the micelle, forming a Stern layer.[10,13,15−17]

Unfortunately, no single experimental technique has yet presented a complete account of the physicochemical properties of a micelle in solution. This is because either the experimental measurements are indirect (e.g., conductivity, NMR, or measurement of transport properties) and require substantial interpretation to extract the micelle properties or they can only access one length scale of structure (e.g., small angle and light scattering can only see the large-scale structure at limited resolution, and techniques such as fluorescence, molecular spectroscopy, and EPR only measure the local environment of the probe).

In principle all-atom simulation should be able to present a complete picture of the micelle in solution. The issue, however, is that the self-assembly of these systems takes place on time scales (microseconds) not accessible to atomistic simulation. To perform all-atom simulations of a micelle, simulators have resorted to biasing the simulation by preassembling a micelle,[11] by rupturing a bilayer to form one,[18] or by running at a state point (like at a higher temperature) that corresponds to smaller, faster forming micelles.[19] Alternatively, it is possible to simulate self-assembly by sacrificing the atomistic detail of the model. This is achieved in a variety of ways, including by coarse-graining,[19−22] by implicitly simulating the solvent,[23,24] or by using on-lattice models.[25,26]

In this paper we present experimental data from wide *Q*-range neutron diffraction measurements of five separate H/D isotopically substituted 0.4 M C_{10}TAB solutions. The extraction of structural information from a disordered system using neutron diffraction measurement combined with isotope substitution is now a well-established experimental technique.[27,28] The concentration of the solutions measured is above the cmc (0.067 M) and below the concentration at which a 2D hexagonal phase is formed.[29] C_{10}TAB was chosen for this study because, at the time of the measurements, the micelles it forms were at the upper limit of the length scale that was accessible to wide *Q*-range neutron diffraction measurement and amenable to atomistic analysis using reverse structural modeling. These measured data sets are interpreted through a modeling process that produces 3D atomic configurations that are consistent with the measured diffraction data while being constrained by known experimental parameters, such as the density and the geometry of the molecules.

The combination of the neutron diffraction data and reverse structural modeling allows us to present a complete, experimentally determined picture of a micelle and its local environment. The atomistic configurations produced are analyzed to identify the micelle, calculate its physical properties—such as its size, shape, and composition—and to examine the details of the micelle's interaction with the solvent and counterions.

THEORY

In a neutron diffraction experiment the differential scattering cross-section is measured and then calibrated and corrected for background and multiple scattering and inelastic self-scattering to produce the total structure factor $F(Q)$. Q is the magnitude of the momentum transfer vector and is defined as $Q = (4\pi/\lambda) \sin \theta$. $F(Q)$ can be written in terms of the concentration of the atomic constituents of the sample, c_α, and their scattering lengths, b_α (these are available in ref 30):

$$F(Q) = \sum_{\alpha,\beta \geq \alpha} (2 - \delta_{\alpha\beta}) c_\alpha b_\alpha c_\beta b_\beta (S_{\alpha\beta}(Q) - 1) \qquad (1)$$

where the summation runs over the pairs of atom types indicated by the indices α and β in such a way that there is no double counting. The structure factor, $S_{\alpha\beta}(Q)$, is the *Q*-space measure of the structural correlation between the two atomic species α and β and is related to the Fourier transform of the pair correlation function, $G_{\alpha\beta}(r)$, by the equation

$$S_{\alpha\beta}(Q) = 1 + \frac{4\pi\rho_0}{Q} \int_0^\infty r G_{\alpha\beta}(r) \sin(Qr)\, dr \qquad (2)$$

where ρ_0 is the atomic number density. Note that $G_{\alpha\beta}(r) = g_{\alpha\beta}(r) - 1$, where $g_{\alpha\beta}(r)$ is the radial distribution function (RDF).

Isotopes of an atom can have different neutron scattering lengths, such as hydrogen ($b_H = -3.74$ fm) and deuterium ($b_D = 6.67$ fm). By substituting deuterium for hydrogen in a system, we are able to alter the contributions of the different $S_{\alpha\beta}(Q)$ functions to the measured $F(Q)$. Assuming that making an isotopic substitution does not alter the structure of the sample, then from each isotopically substituted sample measured, we gain different structural information about the system. Making measurements on *M* isotopically different samples, we get *M* different $F_i(Q)$ data sets with which to determine $S_{\alpha\beta}(Q)$ and, in turn, $g_{\alpha\beta}(r)$. Often the system is complex and only a few isotopic substitutions are practical, so we have an underdetermined system; we have insufficient $F(Q)$ data sets to determine all the $S_{\alpha\beta}(Q)$ functions. In this case using structural modeling that is refined against the experimental measurements and employs known physicochemical constraints (i.e., the system density, molecular structure, and ionic charge of the components) enables us to extract atomistic structural information about the system.[31]

EXPERIMENTAL METHOD

Decyltrimethylammonium bromide was purchased from Acros Organics (99%) and d_{21}-decyltrimethylammonium bromide ($C_{10}D_{21}N(CH_3)_3Br$) from CDN Isotopes (99.1 atom % D). Both were used without further purification. The solutions were prepared by dissolving the surfactants to make 0.4 M solutions in ultrapure water (resistivity 18 MΩ cm), in D_2O (Sigma-Aldrich, 99.9 atom % D), or in a 1:1 H_2O/D_2O molar ratio mixture (referred to as HD).

Diffraction data were collected on five samples, each with different hydrogen−deuterium isotopic substitutions (see Table 1), using the SANDALS time-of-flight diffractometer at the STFC's ISIS research facility, Rutherford Appleton Laboratories, United Kingdom. SANDALS is designed for measurement of samples containing light elements and covers a *Q* range of 0.1−50 Å^{-1}.

The diffraction measurements were made on 1.4 cm^3 of the sample solutions. The samples were held in null scattering TiZr flat plate cells with a wall thickness of 1 mm, giving a sample thickness of 1 mm exposed to the beam that had a circular profile 30 mm in diameter.

Table 1. Combinations of H/D Isotopic Substitutions Made to the Water or $C_{10}TA^+$ Molecules in Each Sample[a]

sample	water	$C_{10}TA^+$
1	H	D
2	D	D
3	HD	D
4	D	HD
5	D	H

[a] HD indicates a mixture of hydrogen and deuterium substitutions made to that molecular species.

The cells and the standard vanadium plate were loaded into the automatic sample changer. The temperature was maintained at 25 °C, and the measurements of each sample were made for approximately 8 h of counting time.

Table 1 in the Supporting Information shows the relative contribution of the individual partial structure factors to the total structure factor for each sample. The water−water correlations dominate the measured neutron scattering; all samples have a total water−water contribution of greater than 60%. The next most significant contribution is from $C_{10}TA^+$−water correlations, followed by $C_{10}TA^+$−$C_{10}TA^+$ correlations, then by $C_{10}TA^+$−Br, and finally by Br−Br contributions (which are less than 0.25%). Although the water−water and the $C_{10}TA^+$−water correlations make up the majority of the experimental signal, we can determine the structure of the entire system—including correlations not strongly weighted in the diffraction data—because we use constraints on the atom positions due to the system's density and the molecules' sizes and geometries in refining our structural models. In addition, because micelles and large aggregates are present, the inhomogeneity of the system will be apparent in the experimental signal, indicating the size and shape of the aggregates present.

EMPIRICAL POTENTIAL STRUCTURE REFINEMENT ANALYSIS

Empirical potential structure refinement (EPSR)[28,32,33] is a variant of the reverse Monte Carlo (RMC) method[34] that produces 3D configurations of a system of molecules, or atoms, that aim to be as consistent as possible with the measured diffraction data. RMC treats the constituent particles as hard spheres and accepts or rejects the Monte Carlo (MC) moves on the basis of whether the fit to the data is improved, whereas EPSR employs classical pair interaction potentials (the "reference potential") and to this it adds an empirical potential (EP) that is derived from the difference between the measured diffraction data and those calculated from the current configuration in the simulation (see ref 28 for the details of the calculation of the EP). As with standard MC molecular simulation, EPSR requires information such as the system's density and composition and the geometry of the constituent molecules. The configurations are then evolved using a standard MC scheme, with the MC moves accepted or rejected on the basis of the Boltzmann factor $\exp(-(\Delta U_{intra} + 1/(k_BT)[\Delta U_{ref} + \Delta U_{EP}]))$, where ΔU_{intra}, ΔU_{ref}, and ΔU_{EP} are the energy differences between the new and old configurations due to the intramolecular, reference and empirical potentials, respectively. In an iterative process the EP adjusts to push the molecular configurations toward ones that agree with experimentally measured diffraction data.

In contrast to standard classical molecular simulation, EPSR allows the molecules to have intramolecular disorder, reflecting that measured experimentally, through each molecule independently sampling a harmonic potential (see ref 33). As a result, at any specific time each molecule has a geometry different from all the others. For the whole molecule MC moves and rotations the molecules are held rigid.

Table 2. Lennard-Jones Parameters, Charges, and Masses for the Reference Potential Used in the Simulations of the $C_{10}TAB$−Water Solutions

atom type	ε/kJ mol^{-1}	σ/Å	mass/amu	q/e
MH, M	0.2000	2.579	2.0	0.0000
CH	0.2000	3.700	12.0	0.0000
C[1−9,T]	0.2000	3.960	12.0	0.0000
N	0.2000	3.200	14.0	+1.0000
Br	0.5659	4.650	80.0	−1.0000
OW	0.6500	3.165	16.0	−0.8476
HW	0.0000	0.000	2.0	+0.4238

Table 3. Intramolecular Bond Average Distances, $d_{\alpha\beta}$

bond	$d_{\alpha\beta}$/Å
C10TA$^+$	
C−N	1.34
C−C	1.53
C−H/D	1.10
Water	
OW−HW	0.976

In this study the intermolecular reference potential for water was based on the parameters from the widely used SPC/E potential.[35] The $C_{10}TA^+$ parameters were based on the OPLS-AA potential,[36] and the bromide parameters were taken from ref 37. Table 2 contains the Lennard-Jones parameters and charges for the intermolecular interactions used in the reference potential. The atom labels used in Table 2, and throughout this paper, indicate the following: N refers to the nitrogen atom in the surfactant headgroup; the carbon atoms in the headgroup are CH, and their hydrogen atoms are labeled MH; the carbon atom in the tail bonded to the nitrogen atom is labeled CT, and the others down the tail are labeled C9 to C1, with C1 furthest away from the headgroup; the hydrogen atoms bonded to the carbon atoms in the tail are labeled M; Br indicates the bromide ions; OW and HW refer to the oxygen and hydrogen atoms of the water molecules. All interaction potentials in the simulation are truncated by being smoothed to zero between 17 and 20 Å.

The intramolecular bond averages used are presented in Table 3. Rotation groups were defined about each carbon−carbon or carbon−nitrogen bond in the $C_{10}TA^+$ molecule.

To improve the statistics, five separate simulations were run, each starting from a different disordered configuration. The composition of the system was set to match the experimental system: 64 $C_{10}TA^+$ molecules and their bromide counterions and 7808 water molecules in a box with sides of length 64.07 Å. The simulations were run at a temperature of 25 °C to match the experimental data.

In addition to the simulations containing 64 surfactants, we ran two other sizes of simulation that contained 56 and 72 $C_{10}TA^+$ and bromide ions and the corresponding number of water molecules to give a concentration of 0.4 M. The results presented are solely calculated from the 64 surfactant simulations, except when

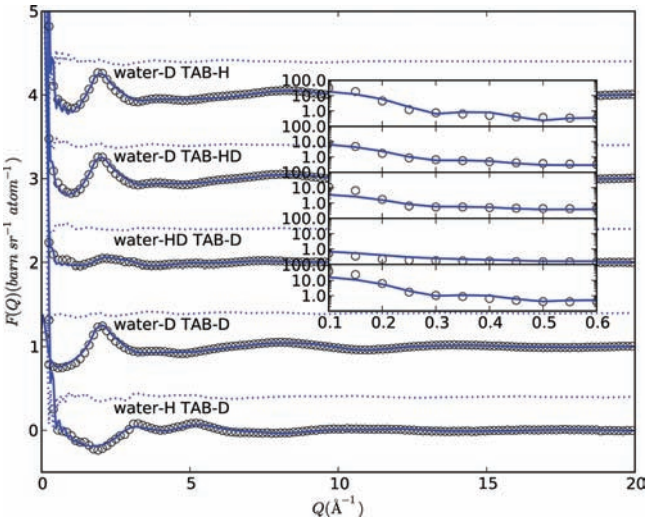

Figure 1. EPSR model fits (solid blue lines) and fit residuals (dashed lines by 1.0 up the ordinate axis) to the diffraction data (black circles) of the five isotopic samples. For clarity, each data set is offset up the ordinate, and each residual from its data set, and also only every fifth experimental data point is plotted. The inset shows the model fits and experimental data in the low-Q region using a log scale on the ordinate axis.

discussions of finite size effects are required, we make reference to findings from the 56 and 72 surfactant simulations.

In EPSR, the $S_{\alpha\beta}(Q)$ functions—which form the $F(Q)$ functions—are computed from the sine transform of the pair correlation functions, $G_{\alpha\beta}(r)$, that are calculated from the atomic configurations produced by the simulation (see eq 2). As is standard in liquid simulation, EPSR uses periodic boundary conditions to attempt to approximate a bulk system. Unfortunately, as a result, if we have structural correlations in our system that persist out to half the simulation box length, $L/2$, then these will be apparent in the $G(r)$ values and consequently cause significant oscillations in the $S(Q)$—and in turn the $F(Q)$—calculated from the simulation.

Since we have large aggregates in these micelle simulations, which approach the length scale of $L/2$, we observe oscillations at low Q in the computed $F(Q)$. Figure 1 in the Supporting Information shows the oscillations in the $F(Q)$ values corresponding to the water-D TAB-H $F(Q)$ sample calculated from three different sizes of simulation of C_{10}TAB solutions. The calculated $F(Q)$ functions corresponding to the water-D TAB-H sample show the largest finite size effect oscillations as they have the largest contrast between the solvent and the micelle. The wavelength of these oscillations corresponds to 2π divided by half the box side length. These low-Q oscillations pose a significant problem in determining the long-wavelength limit of the $F(Q)$ values computed from finite sized simulations of disordered systems.[38] The authors of ref 38 suggest a method to reduce these oscillations to reveal the average functional behavior of $F(Q)$ in the low-Q region: In computing the $S(Q)$ values using eq 2, the $G(r)$ values can be "smoothed" toward zero as r approaches $L/2$ through the multiplication by the convergence function, $\alpha(r;R_{cut})$, where

$$\alpha(r;R_{cut}) = \begin{cases} \left(1-\frac{r}{2R_{cut}}\right)^2\left(1+\frac{r}{4R_{cut}}\right) & \text{if} \quad r \le 2R_{cut} \\ 0 \quad \text{if} \quad r > 2R_{cut} \end{cases} \tag{3}$$

Figure 1 in the Supporting Information shows the effect of applying the convergence function, with R_{cut} set to 0.7 times $L/2$, on the calculated $F(Q)$ functions. Different values of R_{cut} were tried, and 0.7 times $L/2$ was found to be a reasonable choice as it allows the general behavior of $F(Q)$ in this region to be observed without altering higher Q features. The use of the convergence function in the calculation of the $S(Q)$ functions from the models is just to aid the comparison of the model $F(Q)$ functions and the experimental data and is not used in the calculation of the empirical potential in the simulation. It should also be noted that the oscillations due to the finite size of the simulation do not affect the simulation because all interaction potentials, including the empirical potential, are truncated to a range of 20 Å well below half the box side length.

Figure 1 shows the experimentally measured $F(Q)$ data sets from the five isotopic samples and the $F(Q)$ functions calculated from the EPSR models using the convergence function. Also shown are the residuals of the difference between the data and the unmodified $F(Q)$ functions calculated from the models. In the main plot the data are presented over the range 0.2 Å^{-1} < Q < 20.0 Å^{-1} to show the important structural features, but were collected over 0.1 Å^{-1} < Q < 50.0 Å^{-1}.

Simulation Procedure. To generate a disordered starting configuration, the molecules are randomly inserted into a simulation box at a density 64 times lower than the experimental density. The low density minimizes the chance of overlaps of the molecules. Then the simulation is run for a number of MC cycles, allowing the energy to equilibrate. Here one MC cycle corresponds to attempting to move every atom, to rotate every rotational group, and to rotate and translate every molecule once. After this, the box is compressed by about 10% and then the simulation run again. This process of squashing and equilibration is repeated until the experimental density is reached.

The simulation is then run using only the reference potential, allowing the energy of the system to equilibrate for at least 5000 MC cycles. Next the refinement against the neutron data is begun by introducing the empirical potential to the simulation. The simulation is run for a period of equilibration of about 5000 refinement cycles (a refinement cycle consists of five full MC cycles plus the recalculation of the empirical potential) or until the system's total energy has equilibrated. After this, the simulation is run, allowing the EP and the various structural measures (the RDFs, coordination numbers, and structure factors) to accumulate.

The aggregation of the surfactant molecules was examined by using a cluster counting program (see the details in the next section) every 50 refinement cycles (or 250 MC cycles). In running EPSR on the SCARF cluster, provided by the STFC's e-Science facility, we were able to perform 400 refinement cycles in 24 h, meaning that the 80 000 refinement cycle simulations presented in this paper took approximately 200 days to complete.

RESULTS AND DISCUSSION

Surfactant Aggregation: How To Identify Micelles. Viewing snapshots of the configuration of the EPSR simulation after quite a short simulation time, it is clear that the surfactant molecules aggregate to form clusters of molecules (see the right-hand plot in Figure 2). It is apparent that the surfactant molecules cluster into micelle-like entities; the surfactant tails are hidden away from the solvent, and the headgroups and counterions form an interface with the solvent.

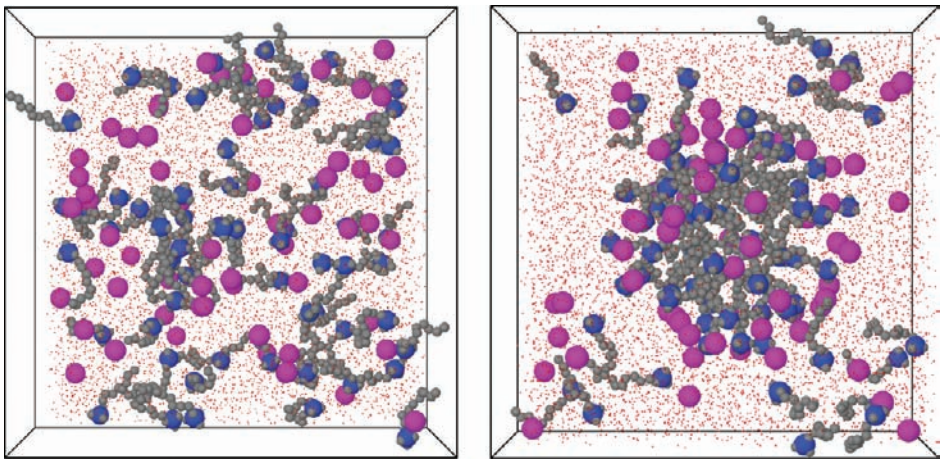

Figure 2. Snapshot of the starting configuration of a 64 C_{10}TAB EPSR simulation (left) and a snapshot once a micelle of 43 surfactant molecules has formed (right). Color scheme: small red spheres are the water molecules' oxygen atoms, the gray spheres are the carbon atoms in C_{10}TAB molecules, the large blue sphere is the nitrogen atom in the headgroup of the C_{10}TAB molecule, and the magenta spheres are the bromide ions. These images were created using the Jmol program.[39]

To identify surfactant clusters and micelles, a scheme that relied on a distance criterion between the carbon atoms in the surfactant tails was used. This was based on that used in Jorge's simulation of C_{10}TAB micelles.[19] Following visual inspection of the largest clusters identified (the micelles), two surfactants were defined to belong in the same cluster if any of the last four carbon atoms in one surfactant's tail are within 5.0 Å of one of the last four carbon atoms in the other surfactant molecule. We found that using cutoffs larger than 5.0 Å tended to identify surfactants that were close to the micelle's surface that were perhaps on their way to, or from, being part of the micelle.

Figure 3 shows the surfactant−surfactant RDFs calculated from the configurations produced by EPSR. The left-hand plot shows the intermolecular RDFs corresponding to carbon atoms at the same position in the surfactant tails; "CT" is the carbon bonded to the nitrogen atom in the headgroup, and "C1" is the one at the end of the tail. The position of the first peak in these RDFs is at increasingly larger distance the further the carbon atom is from the end of the tail. This indicates that the surfactants, in the main, align themselves so that they diverge from a point, as expected in a micelle. For the RDFs of the carbon atoms closest to the end of the tail there is a significant slope to the RDFs enhancing the first and second peaks; this indicates that these atoms occupy a spatially restricted region,[40] like the hydrophobic core of a micelle. This slope decreases the closer the carbon atom is to the headgroup.

The bottom left-hand plot of Figure 3 shows the RDFs corresponding to all 16 permutations of the pair correlation functions between the last four carbon atoms in the tail. It is these last four carbon atoms that are used to define the surfactant clusters in the simulation. The dashed vertical lines in the left-hand plots of the figure correspond to the distance cutoffs used in the cluster analysis. It is apparent that this cutoff captures contacts between the carbon atoms close to the end of the tail and less so for the carbon atoms closer to the headgroup. The RDFs involving the last carbon atom in the tail (the black dashed lines in the bottom left-hand plot) show a significant correlation below this cutoff of 5 Å.

The top right-hand plot in Figure 3 shows the RDFs between the nitrogen atom and the carbon atoms in the surfactant tail. The RDFs between the nitrogen atom and the carbon atoms at the end of the tail away from the headgroup have a more well-defined peak at a shorter distance than for those RDFs involving carbon atoms closer to the headgroup. This difference is due to the steric hindrance of the headgroup, and it indicates that there are some nonparallel contacts between surfactant molecules.

The headgroup−headgroup RDFs (bottom left-hand plot of Figure 3) all have a very broad main peak located at about 9 Å, but they all also show a significant shoulder on this peak, indicating some close contacts.

Simulation Equilibration and Cluster Evolution. We are interested in the configurations that best represent the measured diffraction data. We know that in the real system there are micelles as we are at a concentration above the cmc. We know that the self-assembly process of forming a micelle takes place on the microsecond time scale and that typical atomistic MD simulations probe the nanosecond time scale. In EPSR we use MC moves to evolve the configurations, so although we do not have a real time scale, we know we are sampling phase space at roughly the same rate as an equivalent MD simulation, and so consequently, we expect the formation of a micelle to take a significant amount of simulation time.

EPSR calculates a parameter known as the *R* factor that indicates the quality of the fit of the EPSR model to the data; the lower the *R* factor the better the fit.[33] The bottom plot in Figure 4 shows the evolution of the *R* factor for each of the five EPSR simulations run as a function of the number of refinement cycles. We can see that by approximately the 30000th refinement cycle the *R* values have reached a plateau and do not drop any further. Therefore, we can say that beyond this point the configurations produced by EPSR are as representative of the measured diffraction data as the model is capable of producing. For comparison, running the simulation without refining against the experimental data, the *R* value never drops below a value of 1.6.

Figure 4 also shows the evolution of various properties of the surfactant clusters over the course of the simulations. From the start to about 35 000 iterations the micelles assemble: the size of the largest cluster and the largest clusters (top and second from top plots) increase, the number of monomers (third plot from top) and the number of clusters (fourth plot from top) decrease,

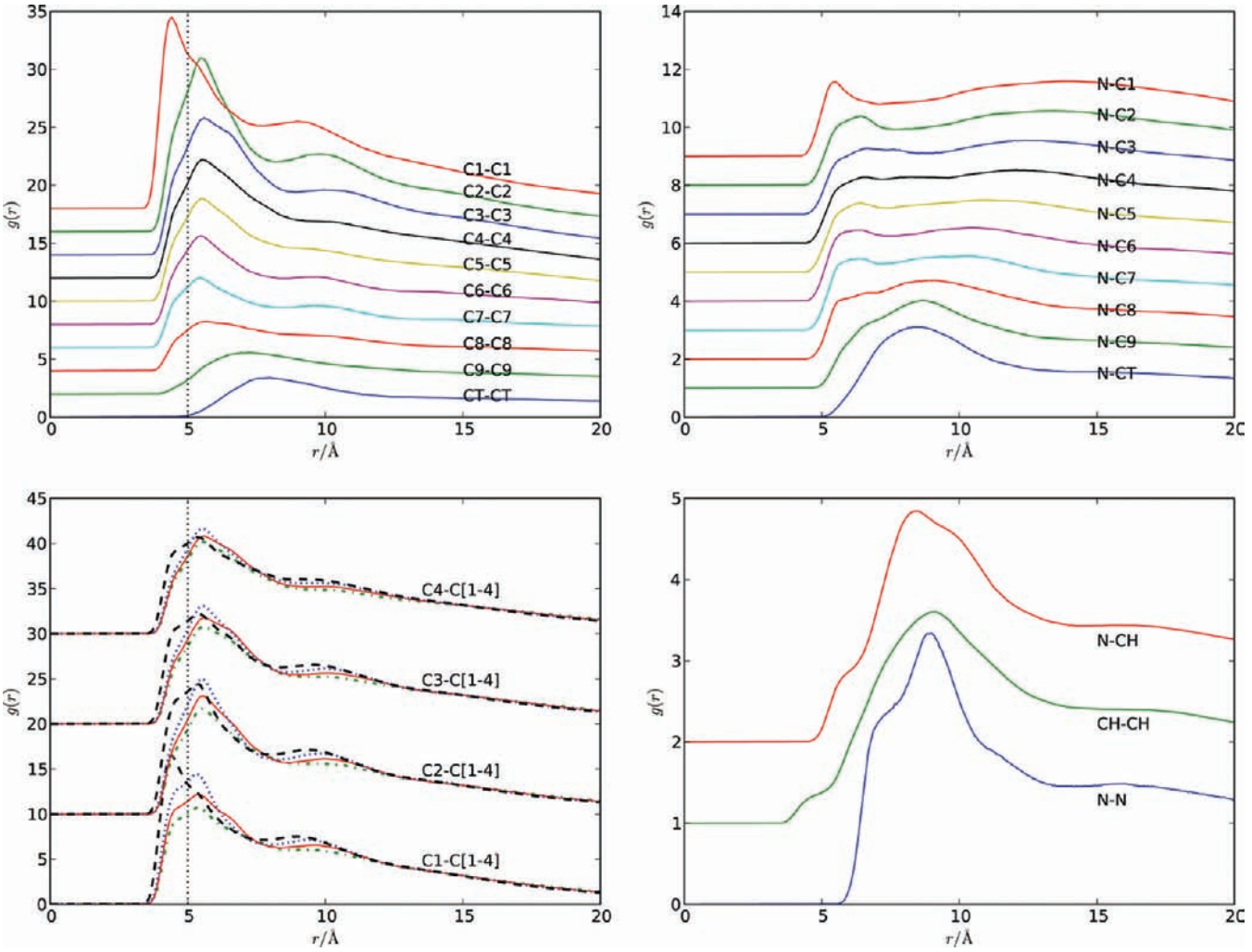

Figure 3. Surfactant−surfactant RDFs: the top left-hand plot shows the RDFs between the carbon atoms in the surfactant tail along the length of the tail, the bottom left-hand plot shows the RDFs of the 16 permutations of pair correlations of the last four carbon atoms in the tail (color scheme: the black dashed line is the C*−C1 RDF, the blue dotted line is the C*−C2 RDF, the red solid line is the C*−C3 RDF, and the green dashed−dotted line is the C*−C4 RDF), the top right-hand plot shows the RDFs between the nitrogen atom and the carbon atoms down the surfactant tail, and the bottom right-hand plot shows the headgroup−headgroup RDFs. For clarity the RDFs are offset by 1.0 up the ordinate. Also shown in the tail−tail plots is a dashed vertical line corresponding to the cutoff used in the cluster criteria.

and the average cluster size drifts upward to a plateau (fifth plot from top). It is worth noting that the surfactants have aggregated significantly in the squashing and equilibration part of the simulation not shown in Figure 4.

We can see in the plot of the evolution of the largest cluster size that one of the simulations (the blue line) forms a large cluster of about 48 $C_{10}TA^+$ molecules much more quickly than the other simulations. The other four simulations seem to follow almost identical processes of assembly, forming a largest cluster of about 44 surfactant molecules. It is quite remarkable that the surfactants assemble to form large micelles over this simulation time; this demonstrates that refining against experimental data accelerates structural equilibration by a factor of greater than 100 in simulation time.

To ensure that we are sampling configurations that best represent the data measured and that the simulation has equilibrated to a steady state, the analysis of structural properties is only performed on the configurations generated after 40 000 refinement cycles.

Properties of Micelles. Having decided upon a method of identifying the surfactant aggregates, we now turn to analyzing their properties. The top plot in Figure 5 shows the distribution of the surfactant cluster sizes averaged over the equilibrated part of the five independent simulations. $f(i)$ is the frequency of observing a cluster of size i molecules, and note that the scale of the ordinate is logarithmic. From the size distribution we can see that the surfactant molecules exist either as monomers or in small clusters (of six or fewer) or as part of a large cluster containing between 39 and 50 surfactant molecules. These large clusters are the micelles.

This split in the distribution of the cluster sizes between micelle-sized aggregates and the monomers and small clusters is consistent with the accepted model of micellization. The idea is that, in solutions where the surfactant concentration is above the cmc, the proportion of surfactants existing as part of a micelle is equal to the excess concentration of surfactant above the cmc, with the rest (equal to the cmc) existing as monomers or in small aggregates. This split in the cluster distribution has been observed in simulation studies (atomistic,[19] implicit-solvent,[24] and on-lattice[26]).

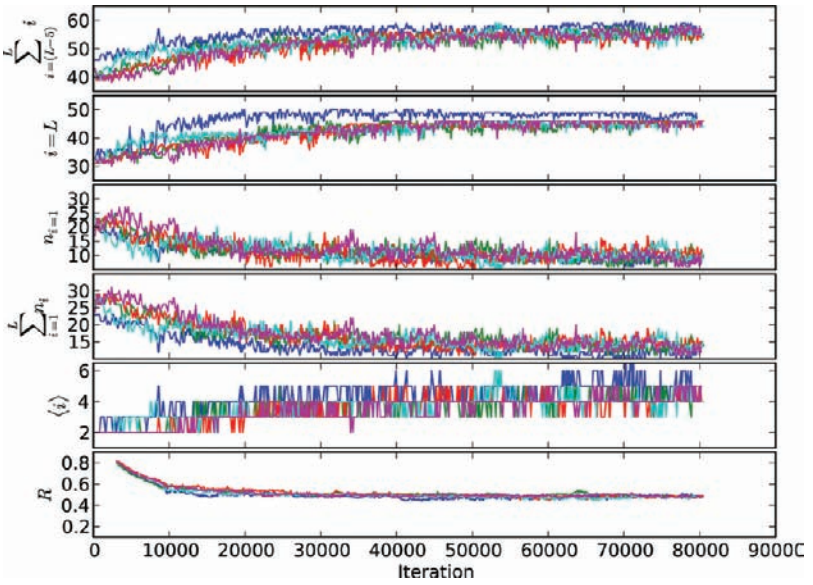

Figure 4. Evolution of the cluster properties and the fit of the model to the measured data over the course of the simulations. The abscissa is the number of refinement cycles completed, and the different color lines correspond to the five independent simulations. The graphs show the various properties of the C_{10}TAB clusters over the course of the simulation, in order from the top: the sum of the sizes of the five largest TAB clusters in the simulation ($\sum_{i=(L-5)}^{L} i$), the size of the largest TAB cluster ($i = L$), the number of monomers ($n_{i=1}$), the total number of clusters ($\sum_{i=1}^{L} n_i$), the average cluster size ($\langle i \rangle$), and finally the R factor. The simulations had been run for a period of at least 10 000 iterations for equilibration prior to the data presented in this figure.

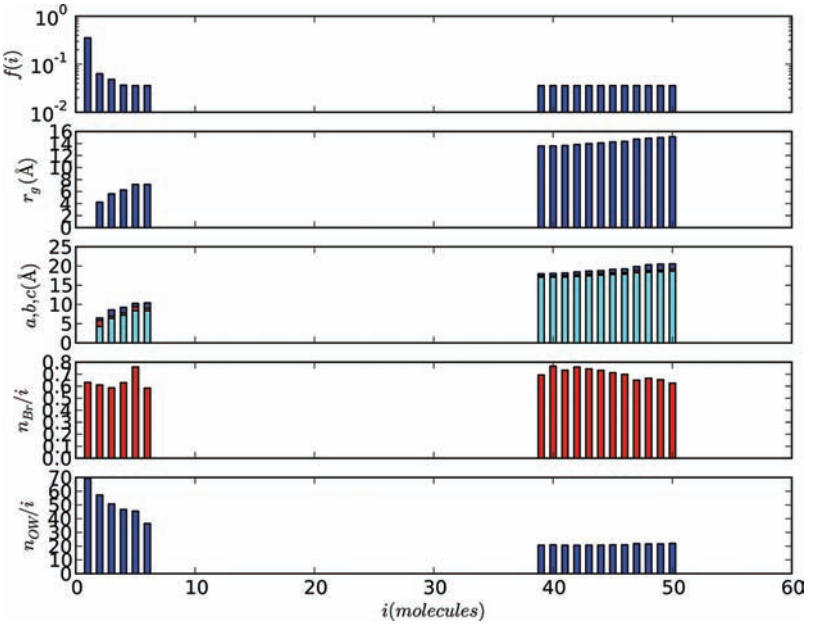

Figure 5. Size distribution of the C_{10}TAB clusters (top plot) and properties of the clusters as a function of size, from top to bottom: the radius of gyration, the clusters semiaxes (from largest to smallest the colors are blue, red, and cyan), the number of bromide ions per surfactant within 5.1 Å of the micelle, and the number of water oxygen atoms with 4.6 Å of the micelle. These data were collected after the simulation had equilibrated (from 40 000 iterations in Figure 4).

Averaging over all cluster sizes gives an average cluster size of 20 surfactant molecules, while averaging over clusters of 10 surfactant molecules or more gives an average of 44.5 surfactant molecules. An average of 44.5 surfactant molecules sits comfortably in the range given in the literature for C_{10}TAB micelles (37[13] to 50[11,17]).

The largest micelle size, reported in refs 11 and 17, was estimated from the molecular weights measured by light scattering[12] and mass spectrometry,[41] but excluding the counterions in the calculation. Other experimental studies report values of around 40 C_{10}TAB molecules: 37 molecules from light scattering,[13] 38 molecules with a distribution width of 6.1 estimated by fitting ultrasound absorption spectra,[10] Evans et al. reported measurements on dye diffusion in the micelle solutions giving an average aggregation number of 40,[42] and Dorrance et al. found from fluorescence studies that an aggregation number of 40 molecules was also observed.[43]

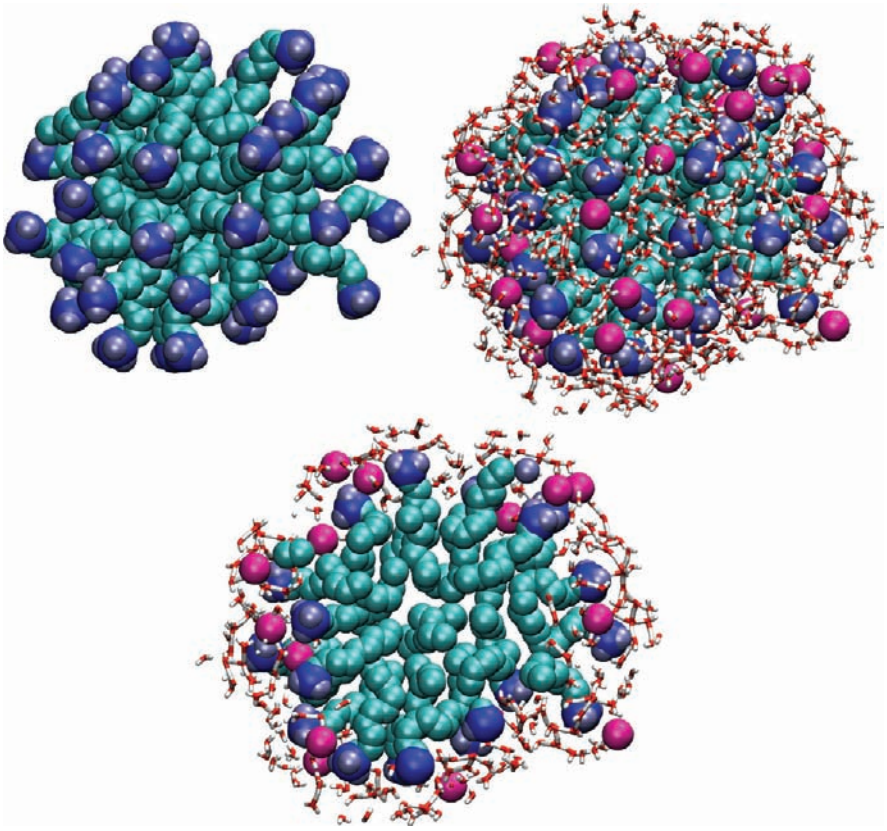

Figure 6. Pictures of a 43 surfactant micelle: the top left image shows just the surfactant molecules, the top right image shows the micelle surrounded by bromide counterions and water molecules, and the bottom image shows the same micelle but in cross-section of 12 Å in width. These images were created using the VMD program.[48]

We find that for the micelle-sized clusters there is a range of cluster sizes that are observed—39−50 surfactant molecules—this might be interpreted as a polydispersity of approximately 12% ((44.5−39)/44.5). It is also possible to make a crude estimate of the cmc from the distribution of cluster sizes. Taking an average micelle size of 44.5 surfactant molecules, this leaves 64 − 44.5 = 19.5 nonmicelle surfactant molecules (assuming one micelle per configuration), which as a proportion of the concentration is (19.5/64) × 0.40 = 0.12 M. This is higher than the experimentally known value of 0.067 M for the cmc. Jorge et al., using the same method on simulations at the higher temperature of 353 K, calculated cmc's of 0.027 (all-atom) and 0.051 (coarse-grained), which are lower than the corresponding experimental value of 0.085 M.[19]

It is worth pointing out that estimating properties like polydispersity and cmc from simulations of this size can be problematic as we have relatively poor statistics—we only have one micelle in each simulation configuration—and these properties are dependent on the system size. In Table 2 in the Supporting Information we present a comparison of micelle properties from the three different simulation sizes that we ran. The smallest simulation (containing 56 surfactants) formed a micelle with an average size of 39 surfactant molecules, and the two larger simulations (of 64 and 72 surfactants) formed an almost identical micelle in its average size, range of sizes found, and shape. We estimate the cmc of the largest simulation to be 0.15 M, which is larger than that from the two smaller simulation sizes of 0.12 M. The 64 and 72 surfactant simulations form a micelle of the same size, so in the 72 TAB simulation, the additional 8 surfactant molecules can only be counted as nonmicelle and so produce a larger cmc estimate.

Figure 5 also shows the variation of the radius of gyration (r_g) and the semiaxes of the clusters as a function of the cluster size. By calculating the moment of inertia tensor for each cluster, and then diagonalizing it, the principal moments of the cluster are available. Then, assuming that the cluster is ellipsoidal, the semiaxes (a, b, and c) of the cluster can be calculated from the principal moments using the relations

$$a = \sqrt{\frac{5}{2}\frac{I_{yy} + I_{zz} - I_{xx}}{M}} \tag{4}$$

$$b = \sqrt{\frac{5}{2}\frac{I_{zz} + I_{xx} - I_{yy}}{M}} \tag{5}$$

$$c = \sqrt{\frac{5}{2}\frac{I_{xx} + I_{yy} - I_{zz}}{M}} \tag{6}$$

where the principal moments are ordered in size such that $I_{xx} \leq I_{yy} \leq I_{zz}$ and M is the mass of the cluster. (Note that the equation of the ellipsoid is $x^2/a^2 + y^2/b^2 + z^2/c^2 = 1$ and that $r_g = (I_{xx} + I_{yy} + I_{zz})^{1/2}$). Figure 5 shows that the radius of gyration increases with the cluster size. For the large clusters, the micelle-sized clusters, the radius of gyration only increases slightly with increasing cluster size, and the average for these is 14.2 Å. Interestingly, the calculated semiaxes are similar for the micelle-sized clusters, meaning the micelles are almost spherical. As the micelles increase in size, the difference in size of the largest semiaxis and the other two increases, indicating that the micelle

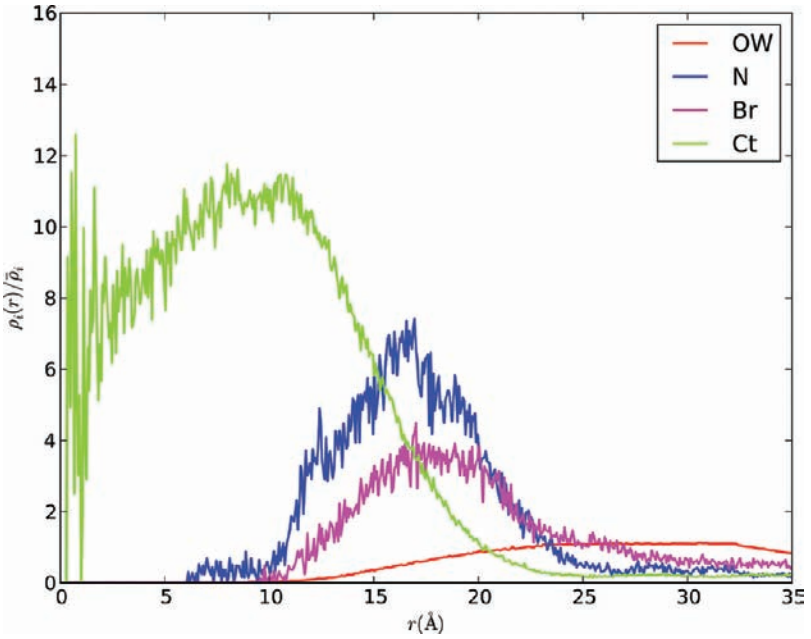

Figure 7. ADPs of various atom types from the center of mass of clusters containing more than 10 surfactants.

becomes more ellipsoidal. The average *a*, *b*, and *c* calculated for the micelles are 19.1, 18.2, and 17.8 Å, respectively.

The radius of gyration and the size indicated by the semiaxes calculated are in good agreement with those determined in other experimental studies of C_{10}TAB: NMR[14] and NMR combined with conductance measurements[15] give a micelle radius of about 17.7 Å. The radius of C_{12}TAB micelles have been estimated as 20.95 Å by fluorescence and EPR,[44] 21.3 Å by SANS,[45] and between 22.1 and 26.03 Å by a later SANS study[46] (Berr et al. assumed that the micelle was ellipsoidal, hence the range in the radius). From the Tanford relation,[47] the extra two alkyl groups make the C_{12}TAB tails 2.54 Å longer than those of C_{10}TAB, and this accounts for most of the difference in the reported radii of the C_{12}TAB and C_{10}TAB micelles.

The shape of the C_{10}TAB micelle is widely considered to be spherical as the light scattering studies found no angular dependence of the scattered light intensity.[12,13] As mentioned above, some small angle scattering studies employ an ellipsoidal model for the TAB micelles.[46] In small angle scattering it is difficult to distinguish between a slightly ellipsoidal micelle and polydispersity of spherical micelles.[45,46] The ratio of the major to the minor axes reported by Hayter et al. is 1.07, meaning that they are pretty spherical. We find an average of 1.06 ± 0.02 for this ratio calculated over all micelles. We find that the largest micelles in the range of sizes we found tend to be slightly more ellipsoidal than the smaller ones.

Defining a Stern layer is key to many of the models of micelles used in both theory and interpretation of experimental measurement. The bottom two plots in Figure 5 show the number of bromide ions and water oxygen atoms within the cutoff distances of 5.1 and 4.6 Å, respectively, of any carbon atom in the surfactant molecules in the cluster as a function of cluster size. The cutoffs used correspond to the trough after the first peak in the corresponding RDF (see Figure 8). The bromide ions identified this way are considered to form the Stern layer.

It is found that the number of water molecules per surfactant hydrating the micelle-sized clusters is reasonably constant at 21.0 molecules. For the micelles, the number of bromide ions per surfactant is also approximately constant around an average of 0.70 atoms per surfactant. The top right-hand picture in Figure 6 shows a micelle surrounded by these water molecules and bromide ions within the cutoff distance. Also shown in Figure 6 is a slice 6 Å either side of the center of mass of the micelle. This cross-section shows the dry hydrophobic core composed of only the tail alkyl groups and outside of this the polar shell region. This outer shell is quite disordered, with the bromide ions and water molecules penetrating beyond the surfactants' headgroups to make contact with some of the alkyl groups close to the headgroup.

To examine the structure of the micelle in cross-section, we plot the radial variation of the atomic density of various atom types as a function of their distance from the center of mass of the micelle. These atomic density profiles (ADPs), shown in Figure 7, have been normalized by the atomic number density of that atom type in the simulation and are averaged over all aggregates containing 10 or more surfactant molecules.

The ADPs show that the micelle consists of a hydrophobic core containing only the surfactant tails (the green line is any tail carbon atom), which extends out to about 10 Å from the center. From here outward, we can see the polar shell that surrounds the micelle—a diffuse region containing surfactant headgroups (the blue line corresponds to the surfactants' nitrogen atom), some surfactant tail groups, water molecules (the red line), and bromide ions (the magenta line). These bromide counterions in this region form the Stern layer around the micelle. This interface region extends out to about 25 Å from the center of the micelle. The peak in the distribution of the nitrogen atoms is at about 17 Å from the center, and the peak in the bromide ion distribution is a few angstroms further out, indicating that the bromide ions form the Stern layer just outside the headgroups. The water is seen to penetrate deeply into this region, but no further than the bromide counterions.

The hydrophobic core region extends out to about 10 Å from the micelle center, while the Tanford length for C_{10}TAB is 14.24 Å, implying that the surfactant tails are not fully elongated and that

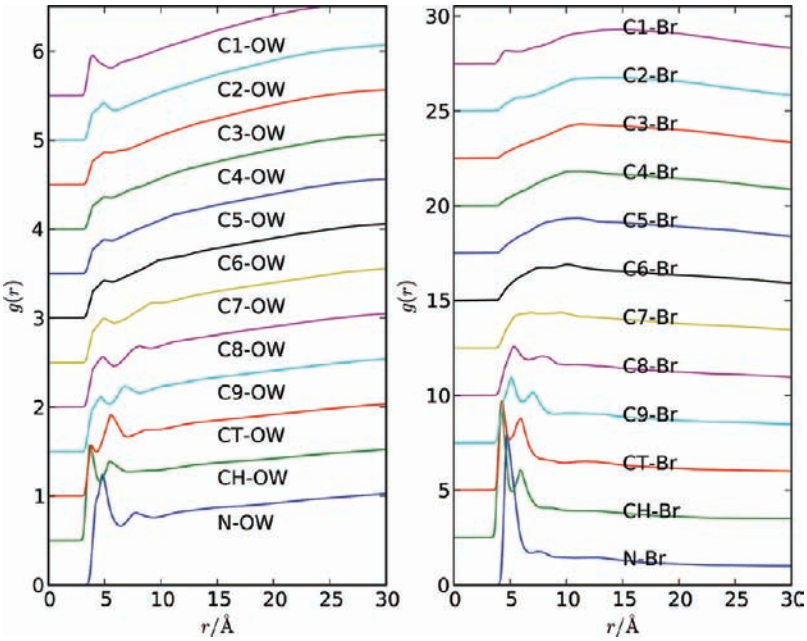

Figure 8. Surfactant−water (left) and surfactant−bromide RDFs. The RDFs have been offset from each other for clarity.

some of the alkyl groups are present in the outer shell region. This is indeed observed in the picture of the cross-section of the micelle in Figure 6.

Perhaps the most remarkable feature of Figure 7 is the width of the outer polar shell that interfaces with the solution. Again, taking the positions of the nitrogen atom in the headgroup (blue line) as indicative of the outer shell, the outer shell could be considered to occupy from 10 Å out to 25 Å, making the shell width 15 Å. A better estimate is the width at the half-height-maximum, which would give a width of about 7.5 Å. For experimental studies that report the polar shell thickness they used, or calculated, for their models of C_{10}TAB micelles, there is little agreement; but our value of 7.5 Å sits well within the range of values. In interpreting neutron reflectometry measurements of C_nTABs at the air−water interface, Gaussian functions of width 10.5 ± 3.0 Å were used to model the interface region containing the headgroups.[49] While for models used in interpreting SANS experiments on C_{12}TAB micelles there was not much consensus, the polar layer was found to be 4.5 Å[45] and 9.0 Å[46] thick.

Other experimental models instead report the thickness of the Stern layer, and all the estimates are substantially narrower than that shown by the bromide ADP function, which has a width at half-maximum of about 7.5 Å. The Stern layer thickness for C_{10}TAB micelles was estimated from NMR measurement to be 3.5 Å,[14,15] while in their fluorescence and EPR study of C_{12}TAB micelles Bales et al. used an outer shell thickness of 5.35 Å.[44]

In many models of micelles the number of alkyl groups not in the hydrophobic core—the "wet" alkyl groups, N_{wet}—is commonly reported, but—once again—there is little agreement on what this should be. Some models make it a function of the number of surfactants in the micelle, while some set it to be anywhere between 0 and 4. While we have not explicitly calculated N_{wet}, it is clear from the ADPs and the snapshots of the micelles that there are a significant number of alkyl groups in the polar shell of the micelle.

It is clear that the polar shell of the micelle has significant disorder and that the Stern layer is not a thin, well-defined shell. It should be noted, however, that the ADPs have been averaged over micelles that range in size from 39 to 50 surfactant molecules, so the width of the polar region and Stern layer reflects the ensemble average.

The atomic density profiles corresponding to the polar shell calculated in this study agree almost perfectly with the MD simulations of C_{10}TAB micelles.[11,19] Our study gave close agreement in the position and width of the headgroup and bromide ADPs calculated from Pal et al.'s simulation of a preassembled micelle containing 47 surfactants. The widths of headgroup and bromide ADPs calculated by Jorge in his simulations were similar to ours, but the positions of the headgroup and bromide regions were at smaller distances since they investigated a higher temperature than in our study, which produced smaller, more disordered micelles.

The surfactant−water RDFs in Figure 8 show a first nearest neighbor peak indicating that there is contact between water and the carbon atoms along the surfactant tail. This peak diminishes and the RDFs' get an increasing upward slope the further away from the headgroup the carbon atom is. This indicates that the dominant contact of the surfactant with the solvent is through the headgroups and the carbon atoms close to the headgroup and that the parts of the tail furthest from the headgroup are segregated away from the water.

We know from the ADPs in Figure 7 that water does not enter the dry hydrophobic core of the micelle, but the RDFs in Figure 8 indicate that there are some first nearest neighbor contacts between the water and the tail groups furthest down the tail. This signal in the RDFs will mostly be from the fraction of surfactant molecules not part of the micelle that are "free floating" in solution.

The location and number of bromide counterions in the polar shell region is of particular interest due to their effect on the morphology of the micelle. The surfactant−bromide RDFs in Figure 8 indicate that the surfactants' contact with the bromide ion is mostly through the headgroup and not the hydrophobic tails. The peaks in the C9−Br and C8−Br RDFs are just

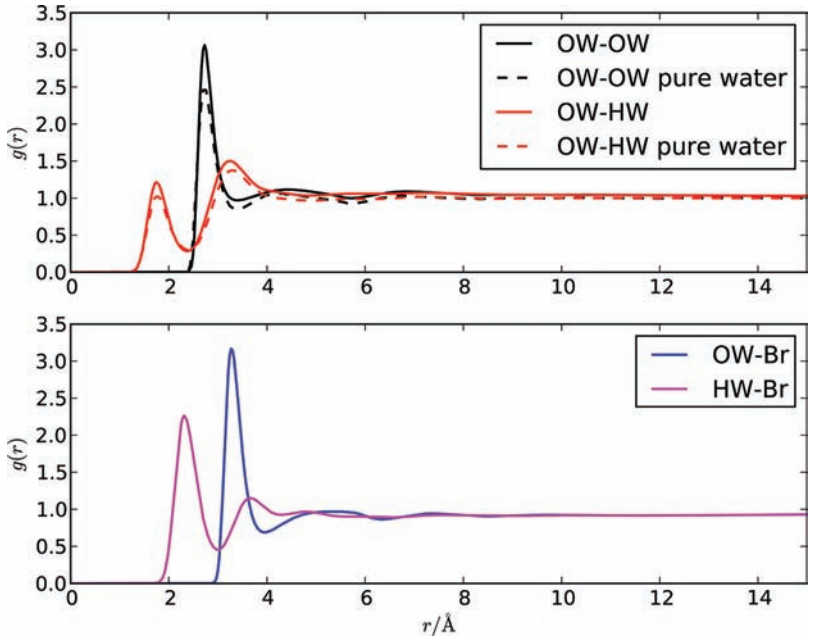

Figure 9. Water−water and Br−water RDFs. The top figure also includes the RDFs from a pure water EPSR study.[52].

reflections of the peaks in the CH−Br and CT−Br RDFs. Our findings support the very detailed analysis of ref 50, and we conclude that the bromide ions do not penetrate into the micelle significantly beyond the CT group. The broad range of distances that the bromide ions occupy from the center of the micelle, shown in the bromide ADP in Figure 7, is due to the variation in the distances of surfactant headgroups from the micelle's center, and not due to the ions penetrating far into the micelle. In fact, the peak position of the bromide ADP (at approximately 18.0 Å) indicates that they tend to sit just outside the surfactant headgroups. All of this verifies the pictures of the micelle and its Stern layer shown in Figure 6.

The fraction of dissociated counterions, β, is an important quantity used in many models of micellization[47,51] and in the interpretation of experimental data.[44−46] In ionic surfactants the counterions allow the headgroups, which would normally repel each other, to pack more closely together. The plot second from the bottom in Figure 5 shows the number of bromide ions per surfactant as a function of the cluster size. Averaging over the micelle-sized clusters gives a value of 0.7 bromide ions. Subtracting this from 1 gives an estimate for the value of β of 0.3. This sits in the middle of the range of the β values (0.22−0.42) reported in other experimental studies of C_{10}TAB micelles.[10,13,15−17] The first peak coordination numbers of the bromide−nitrogen atom RDFs can be used to calculate β, giving a value of 0.2. The simulation studies have calculated β from the RDFs, and these range between 0.19 and 0.43.[11,19] However, calculating β from the RDFs underestimates it as the RDFs are averaged over all surfactants, and we believe it is better to calculate β by actually interrogating the local environment of the micelles.

From the picture of the Stern layer in Figure 6, it seems as if the bromide ions in the Stern layer maintain their hydration shells. This is corroborated by the first peak coordination number of the Br−OW RDF, which is 6.1 atoms; this is only slightly lower than the coordination number reported in the EXAFS study of dilute rubidium bromide solutions of 6.3.[37] From the bottom plot in Figure 9 it is clear that the water molecules surrounding the bromide ion point their hydrogen atoms at the ion. Also shown in Figure 9 are the water−water RDFs measured in this study and those from experimental pure water.[52] It is apparent that the water in the C_{10}TAB solutions looks similar to pure water; the locations of the peaks in the RDFs are almost the same as those of pure water, and the peak heights are only different as a result of the lower density of the solutions as their coordination numbers are maintained (the OWOW first peak is 4.4 compared with 4.3 in pure water).

CONCLUSIONS

Through the use of wide Q-range neutron diffraction measurement on isotopically substituted samples—interpreted through EPSR modeling—we have created atomistic configurations of a micelle and its surrounding environment in solution. We believe that this is the first time a complete atomistic structural picture of a micelle in solution has been experimentally determined and that this study shows the value of using wide Q-range neutron diffraction to study systems with mesoscopic structure.

Unlike in many molecular modeling studies, we found there was no need to bias the structural model as a micelle spontaneously assembled from an initially disordered configuration in the process of refining against the experimental data.

The general properties of the micelles we have calculated are in good agreement with those reported in the literature. The number of surfactant molecules in the micelles varied between 39 and 50 molecules, with an average of 44.5 molecules. The micelles were found to be fairly spherical with a radius of gyration of 14.2 Å and the ratio of the major to the minor axes was only 1.06. The larger micelles were found to be more elliptical that the smaller ones. Examining the cross-sectional structure of the micelle revealed a hydrophobic core about 10 Å in radius. This "dry" core was surrounded by a polar shell of thickness about 7.5 Å, which contained the surfactant headgroups, a number of the alkyl groups from the surfactant tails, bromide ions, and some

water. Totals of 0.7 bromide ions and 21 water molecules per surfactant were found in this outer region. It appears that the bromide ions in the Stern layer maintain their hydration shell of approximately six water molecules.

The thickness of the micelle's corona is one of the key variables in the interpretation of SANS data. Consequently, it was interesting to note that the value of the corona thickness we estimate corresponds well with the range of thicknesses (4.5−9.0 Å) used in SANS studies.[45,46] We plan to test how well the various micelle properties determined in this study can be used to interpret small angle scattering data.

New atomistic insight will be provided by this technique as it is employed to examine other systems. It is our intention to now use this method to study the origin of the changes in micelle size and shape with different counterions and temperature, investigate the interaction of small inorganic species with the micelle (representing part of the templating process for mesoporous materials), and examine polymer−micelle complexes to understand if the polymer binds to the micelle surface or if it is thread through the center of the structure.[3,53,54]

Advances in the instrumentation for wide Q-range diffraction experiments will provide an even greater Q-range, allowing larger self-assembling systems to be examined at atomic resolution, and reduced counting times will make time-resolved interrogation of processes in solution possible.[55]

■ ASSOCIATED CONTENT

Supporting Information. A table of the relative contributions of the individual partial structure factors to the total structure factor for each sample, a figure showing the oscillations in the structure factor due to the finite size effects and the effect of using a convergence function to reduce them, and a table of micelle properties calculated from three different simulation sizes. This material is available free of charge via the Internet at http://pubs.acs.org.

■ AUTHOR INFORMATION

Corresponding Author
rowan.hargreaves@stfc.ac.uk

■ ACKNOWLEDGMENT

We thank the STFC for beam time (Grant RB620144) and for computing resources provided by the STFC's e-Science facility. R.H. thanks Alan Soper for help in using the EPSR and Gudrun software and in developing the micelle analysis routines.

■ REFERENCES

(1) Myers, D. *Surfactant Science and Technology*; John Wiley & Sons: New York, 1988.
(2) Schramm, L. *Surfactants: Fundamentals and Applications in the Petroleum Industry*; Cambridge University Press: Cambridge, U.K., 2000.
(3) Brackman, J.; Engberts, J. *Chem. Soc. Rev.* **1993**, *22*, 85–92.
(4) Grieser, F.; Drummond, C. J. *J. Phys. Chem.* **1988**, *92*, 5580–5593.
(5) Bonacucina, G.; Cespi, M.; Misici-Falzi, M.; Palmieri, G. F. *J. Pharm. Sci.* **2009**, *98*, 1–42.
(6) Ganta, S.; Devalapally, H.; Shahiwala, A.; Amiji, M. *J. Controlled Release* **2008**, *126*, 187–204.
(7) Edler, K. *Philos. Trans. R. Soc. London, Ser. A* **2004**, *362*, 2635.
(8) Ying, J.; Mehnert, C.; Wong, M. *Angew. Chem., Int. Ed.* **1999**, *38*, 56–77.
(9) Zana, R.; Yiv, S.; Strazielle, C.; Lianos, P. *J. Colloid Interface Sci.* **1981**, *80*, 208–223.
(10) Nomura, H.; Koda, S.; Matsuoka, T.; Hiyama, T.; Shibata, R.; Kato, S. *J. Colloid Interface Sci.* **2000**, *230*, 22–28.
(11) Pal, S.; Bagchi, B.; Balasubramanian, S. *J. Phys. Chem. B* **2005**, *109*, 12879–12890.
(12) Debye, P. *Ann. N.Y. Acad. Sci.* **1949**, *51*, 575–592.
(13) Yoshida, N.; Matsuoka, K.; Moroi, Y. *J. Colloid Interface Sci.* **1997**, *187*, 388–395.
(14) D'Errico, G.; Ortona, O.; Paduano, L.; Vitagliano, V. *J. Colloid Interface Sci.* **2001**, *239*, 264–271.
(15) Ribeiro, A.; Lobo, V.; Valente, A.; Azevedo, E.; Miguel, M.; Burrows, H. *Colloid Polym. Sci.* **2004**, *283*, 277–283.
(16) Evans, D.; Mukherjee, S.; Mitchell, D.; Ninham, B. *J. Colloid Interface Sci.* **1983**, *93*, 184–204.
(17) Chakraborty, I.; Moulik, S. *J. Phys. Chem. B* **2007**, *111*, 3658–3664.
(18) Yang, W.; Wu, R.; Kong, B.; Zhang, X.; Yang, X. *J. Phys. Chem. B* **2009**, *113*, 8332–8338.
(19) Jorge, M. *Langmuir* **2008**, *24*, 5714–5725.
(20) Jun, X.; Wenqi, S.; Ganzuo, L.; Gaoyong, Z. *Chem. Phys. Lett.* **2007**, *438*, 326–329.
(21) Wu, R.; Deng, M.; Kong, B.; Yang, X. *J. Phys. Chem. B* **2009**, *113*, 15010–15016.
(22) Sanders, S.; Panagiotopoulos, A. *J. Chem. Phys.* **2010**, *132*, 114902.
(23) Shinto, H.; Morisada, S.; Miyahara, M.; Higashitani, K. *Langmuir* **2004**, *20*, 2017–2025.
(24) Morisada, S.; Shinto, H. *J. Phys. Chem. B* **2010**, *114*, 6337–6343.
(25) Larson, R. *J. Chem. Phys.* **1988**, *89*, 1642.
(26) Mackie, A.; Panagiotopoulos, A.; Szleifer, I. *Langmuir* **1997**, *13*, 5022–5031.
(27) Enderby, J.; North, D.; Egelstaff, P. *Philos. Mag.* **1966**, *14*, 961–970.
(28) Soper, A. *Phys. Rev. B* **2005**, *72*, 104204.
(29) Fukada, K.; Matsuzaka, Y.; Fujii, M.; Kato, T.; Seimiya, T. *Thermochim. Acta* **1998**, *308*, 159–164.
(30) Sears, V. *Neutron News* **1992**, *3*, 26–37.
(31) Finney, J.; Soper, A. *Chem. Soc. Rev.* **1994**, *23*, 1–10.
(32) Soper, A. K. *Chem. Phys.* **1996**, *202*, 295–306.
(33) Soper, A. *Mol. Phys.* **2001**, *99*, 1503–1516.
(34) McGreevy, R. *J. Phys.: Condens. Matter* **2001**, *13*, R877.
(35) Berendsen, H. J. C.; Grigera, J. R.; Straatsma, T. P. *J. Phys. Chem.* **1987**, *91*, 6269–6271.
(36) Jorgensen, W. L.; Maxwell, D. S.; Tirado-Rives, J. *J. Am. Chem. Soc.* **1996**, *118*, 11225–11236.
(37) Bowron, D. T. *J. Phys.: Conf. Ser.* **2009**, *190*, 012022.
(38) Graff, A.; Thorpe, M. *Acta Crystallogr., Sect. A* **2009**, *66*, 22–31.
(39) Jmol: an open-source Java viewer for chemical structures in 3D, 2011.
(40) Bruni, F.; Ricci, M.; Soper, A. *J. Chem. Phys.* **1998**, *109*, 1478.
(41) Nohara, D.; Bitoh, M. *J. Mass Spectrom.* **2000**, *35*, 1434–1437.
(42) Evans, D.; Allen, M.; Ninham, B.; Fouda, A. *J. Solution Chem.* **1984**, *13*, 87–101.
(43) Dorrance, R.; Hunter, T. *J. Chem. Soc., Faraday Trans. 1* **1974**, *70*, 1572–1580.
(44) Bales, B.; Zana, R. *J. Phys. Chem. B* **2002**, *106*, 1926–1939.
(45) Hayter, J.; Penfold, J. *Colloid Polym. Sci.* **1983**, *261*, 1022–1030.
(46) Berr, S.; Jones, R.; Johnson, J., Jr. *J. Phys. Chem.* **1992**, *96*, 5611–5614.
(47) Hamley, I. *Introduction to Soft Matter*, Rev. Ed; John Wiley & Sons, Chicester, U.K., 2007.
(48) Humphrey, W.; Dalke, A.; Schulten, K. *J. Mol. Graphics* **1996**, *14*, 33–38.
(49) Lu, J.; Thomas, R.; Penfold, J. *Adv. Colloid Interface Sci.* **2000**, *84*, 143–304.

(50) Jorge, M. *J. Mol. Struct.: THEOCHEM* **2010**, *946*, 88–93.
(51) Israelachvili, J.; Mitchell, D.; Ninham, B. *J. Chem. Soc., Faraday Trans. 2* **1976**, *72*, 1525–1568.
(52) Soper, A. K. *J. Physics: Condens. Matter* **2007**, *19*, 335206.
(53) Taylor, D.; Thomas, R.; Penfold, J. *Adv. Colloid Interface Sci* **2007**, *132*, 69–110.
(54) Shang, B. Z.; Wang, Z.; Larson, R. G. *J. Phys. Chem. B* **2009**, *113*, 15170–15180.
(55) Bowron, D. T.; Soper, A. K.; Jones, K.; Ansell, S.; Birch, S.; Norris, J.; Perrott, L.; Riedel, D.; Rhodes, N. J.; Wakefield, S. R.; Botti, A.; Ricci, M.-A.; Grazzi, F.; Zoppi, M. *Rev. Sci. Instrum.* **2010**, *81*, 033905.